# LIMNOLOGY and OCEANOGRAPHY



Limnol. Oceanogr. 67, 2022, 2296–2308
© 2022 The Authors. Limnology and Oceanography published by Wiley Periodicals LLC on behalf of Association for the Sciences of Limnology and Oceanography.

doi: 10.1002/lno.12203

# Characterizing temporal and spatial scales of radiatively driven convection in a deep, ice-free lake

Jay Austin 0,1,2\* Craig Hill 0,1,3 Jacob Fredrickson,1,4 Grace Weber,2 Kaelan Weiss2

<sup>1</sup>Large Lakes Observatory, University of Minnesota Duluth, Duluth, Minnesota

#### **Abstract**

From May to July 2019, an array of moored equipment was deployed in Lake Superior to characterize the spatial and temporal scales of radiatively driven convection (RDC). Previous work suggested that convective plumes have horizontal scales on the order of tens of meters, posing a significant observational challenge. The centerpiece of the deployment was a large, two-dimensional (2D) array of thermistors that provided resolution on the order of 10 meters in both the vertical and a single horizontal dimension. This was augmented by an acoustic Doppler current meter mooring and a meteorology buoy capable of estimating surface heat and momentum fluxes. Instantaneous temperature variability at a given location is dominated by a lateral background flow advecting strong horizontal temperature gradients. By combining velocity data with temperature data, this fact can be used to examine horizontal structure at centimeter scales, and can produce 2D images of instantaneous temperature distribution on a horizontal surface, revealing multiple patterns of temperature anomaly distribution. The walls of convective structures are very sharp, with horizontal gradients on the order of 1°C m<sup>-1</sup>; horizontal scales of convective structures themselves are on the order of many tens of meters. Finally, convection is shown to strongly control the vertical distribution of water quality parameters.

The phenomenon of radiatively driven convection (RDC) in cold (i.e., below the temperature of maximum density,  $3.98^{\circ}$  for fresh water, hereafter  $T_{\rm MD}$ ) freshwater lakes has received attention in recent years, mostly in relatively shallow, ice-covered lakes (Mironov et al. 2002; Jonas et al. 2003; Ulloa et al. 2018), but also in deeper, ice-free lakes (Farmer 1975; Austin 2019; Cannon et al. 2019; Cannon et al. 2021). In the springtime, incident shortwave radiation warms near-surface waters, either through surface ice or directly, producing a statically unstable water column, which then undergoes convective adjustment. This process occurs on diurnal scales, with instability building up during the day and convective

\*Correspondence: jaustin@d.umn.edu

This is an open access article under the terms of the Creative Commons Attribution License, which permits use, distribution and reproduction in any medium, provided the original work is properly cited.

Additional Supporting Information may be found in the online version of this article.

**Author Contribution Statement:** J.A.A. conceived the experiment and did the bulk of the analysis and writing. C.H. oversaw the field deployment. J.F. participated in the initial analysis of data and contributed to the writing. G.W. and K.W. played a significant role in the field deployment and initial analysis of data.

processes homogenizing the water column until after sundown, reaching near-isothermy typically before local midnight (Austin 2019; Cannon et al. 2021). Recently, detail of the structure of the convective cells themselves was explored using observations from both single-point moorings and an autonomous glider deployment in Lake Superior (Austin 2019). Among other results, this study suggested that convective cells consist of a downwelling parcels of anomalously warm water with lateral scales on the order of 10 m, and a gentle upwelling return flow occupying the rest of the water column, with lateral scales on the order of 50–100 m, observed in water approximately 180 m deep. Water warmed at the surface arrives at the bottom of the lake roughly 6 h after sunup, suggesting vertical speeds on the order of 1 cm s $^{-1}$ .

Features with very short horizontal scales pose an observational challenge, as most conventional observational techniques (e.g., single-point moorings, shipboard profilers), are designed to characterize vertical variability rather than lateral. This is a reasonable assumption in many if not most scenarios, where scales of lateral variability are reasonably assumed to be very large compared with scales of vertical variability. Remote sensing is perhaps the primary method for observing lateral variability on short scales, but only makes observations at the surface, and typically has resolution no better than several

<sup>&</sup>lt;sup>2</sup>Department of Physics and Astronomy, University of Minnesota Duluth, Duluth, Minnesota

<sup>&</sup>lt;sup>3</sup>Department of Mechanical and Industrial Engineering, University of Minnesota Duluth, Duluth, Minnesota

<sup>&</sup>lt;sup>4</sup>Water Resources Science Program, University of Minnesota Duluth, Duluth, Minnesota

hundred meters, depending on the parameter. In contrast to arrays of single point moorings (e.g., Boegman et al. 2003; Gomez-Giraldo et al. 2008), which often have lateral separation scales of hundreds to thousands of meters, the data we present here is from a two-point mooring with 10 m resolution in the horizontal. A two-dimensional (2D) mooring like what will be presented here was deployed in Massachusetts Bay to study internal waves (Butman et al. 2006), although the horizontal nature of the mooring received limited use. The engineering properties of the mooring itself were studied as well (Grosenbaugh et al. 2002). We are not aware of other examples of this sort of 2D mooring being used in an oceanographic or limnological context; however, a three-dimensional (3D) array of precision, synchronized thermistors was deployed in 2015 (van Haren et al. 2016), also to study internal waves, followed by a deployment in late 2020 of a very large 3D array consisting of nearly 3000 thermistors, to study internal wave turbulence development in the Mediterranean Sea (van Haren et al. 2021). Another approach for studying short horizontal scales is to use towed or autonomous vehicles. Forrest et al. (2008) interpreted data from an autonomous underwater vehicle (AUV) as horizontal variability associated with convective cells. More recently, Austin (2019) made a similar interpretation of data from an autonomous underwater glider (AUG), attributing spikes in temperature and chlorophyll a (Chl a) fluorescence to downwelling plumes of recently heated water. Both methods (AUVs and AUGs) provide submeter horizontal resolution of the measured fields. In the case of the glider, interpretation of the data is more complicated since the flight path is not horizontal, so that vertical variability can alias results.

The temperature fluctuations associated with this process can appear trivially small, on the order of 0.1°C. However, temperature fluctuations are simply a manifestation of an extremely effective mechanism for mixing the water column, and this mixing has impacts beyond just the temperature field. Vehmaa and Salonen (2009) showed that convection under ice in the late winter resulted in near-uniform distributions of nonmotile diatoms, whereas motile species were able to at least partially overcome the impact of convection and concentrate near the surface. Similarly, Kelley (1997) placed constraints on algal distributions in ice-covered Lake Baikal during RDC. More recently, Yang et al. (2017) demonstrated the impact of convection on the distribution of dissolved oxygen. Finally, recent work (Austin et al. 2022) shows a direct impact of convective redistribution of phytoplankton on zooplankton migratory behavior. In this paper we briefly consider the impact of convection on similar fields during two phases of springtime warming: when the water column is negatively stratified and convection only impacts the upper portion of the water column; and later in the period, when the water column is effectively uniform in temperature and convection mixes the entire 180 m water column on time scales of hours.

Convection is shown to have a first-order impact on the distribution of several water quality parameters, such as dissolved oxygen, chlorophyll concentration, and transmission.

Several features of this deployment distinguish the observations presented here from previous fieldwork addressing RDC. From the perspective of the physical setting, Lake Superior is deep compared to most previous studies of RDC (Lake Venduryskoe, 10 m, Jonas et al. 2003, Volkov et al. 2018; Lake Onego, 24 m, Bouffard et al. 2016, Ulloa et al. 2018; Lake Simcoe, 35 m, Yang et al. 2017). In addition, the RDC season occurs when Superior is largely ice-free, unlike most other studies (likely due to the fact that most other studies focus on shallower lakes, which freeze more readily). The absence of ice results in higher radiative fluxes and exposes the water column to wind. From an observational perspective, we implemented a large, 2D array of thermistors. A two-point mooring spanning 180 m in the horizontal and 150 m in the vertical allows the short lateral scales of convective cells to be studied using approaches unavailable to traditional single point mooring data. In addition to this large mooring, we deployed a high-quality acoustic Doppler current meter (ADCP) and a meteorological buoy with a suite of sensors capable of estimating surface heat flux (SHF) and momentum flux. Combining measurements from these three platforms result in a novel view of the temporal and spatial scales of RDC.

#### Methods

On 06 May 2019, a large array of moored equipment was deployed in the western arm of Lake Superior; equipment was recovered on 16 July 2019. The region chosen is near the long-term NDBC buoy site 45006 (Fig. 1a,b), where the University of Minnesota Duluth's Large Lakes Observatory has occupied the site with subsurface moorings since 2005 (Austin and Elmer 2021), providing long-term thermal context for the region. The water depth was approximately 180 m, and the bathymetry relatively featureless. The site is roughly 60 km offshore, both to the northwest (NW) and to the southeast.

The primary platform was a large two-point mooring (Fig. 1b,c), similar to the design of a mooring deployed in Massachusetts Bay in 1998 (Grosenbaugh et al. 2002). The mooring consisted of two anchors, each with an acoustic release, attached to two diagonal cables, both attached to 1 m diameter steel floats, connected with a 180-m-long "headline," which was at approximately 34 m depth. The headline was instrumented with RBR TR-SOLO thermistors every 10 m. We define a horizontal coordinate system for the mooring such that the thermistor at the far southwest (SW) extent of the mooring is at x=0 m and the one at the far northeast (NE) extent of the mooring is at x=0 m and the one at the far northeast easemblies were suspended at 30 m intervals, each with six more thermistors (in addition to the one at 34 m) at 44, 54,

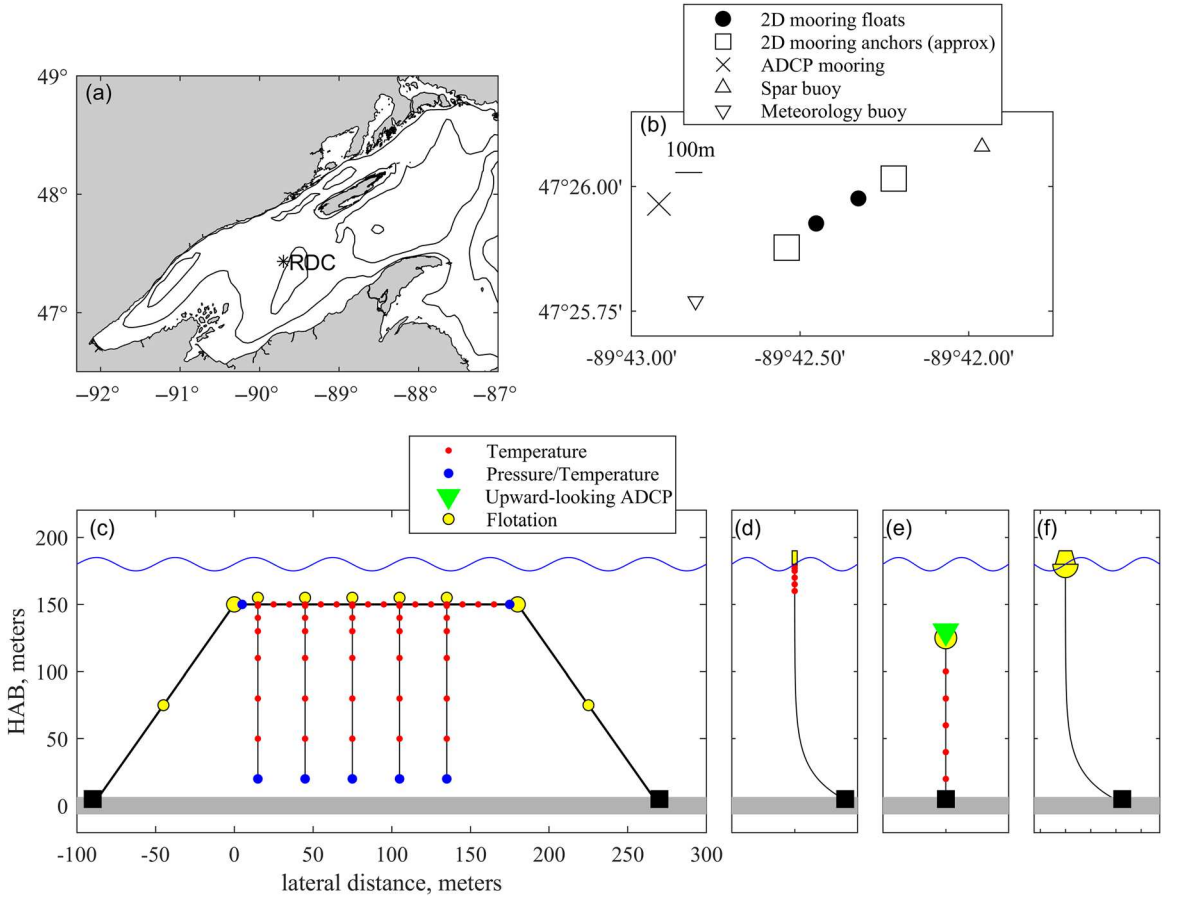


Fig. 1. (a) Location of array in Lake Superior, labeled as RDC. (b) Plan view of array layout. (c) Schematic of horizontal mooring. (d) Spar buoy. (e) ADCP mooring. (f) Meteorology buoy.

74, 104, 134, and 164 m (a sixth line was planned but lost during deployment). All TR-SOLO thermistors on all platforms recorded at 2 Hz. Of the 48 thermistors deployed on the horizontal mooring, 1 failed halfway through the deployment, with the rest returning full datasets. Each vertical line had a  $\sim 30~\rm kg$  steel chain anchor, compensated by flotation where the vertical lines met the headline so that each vertical assembly was effectively neutrally buoyant. A combination of RBR TR-Duet and TR-2050 pressure sensors were placed near both primary floats and at the bottom of each vertical line to determine the motion of the mooring due to currents. Temperature from the TR-2050s is not used in any of our analyses. In short, the mooring was very stiff, with maximum vertical deviations from equilibrium position on the order of tens of centimeters over the course of deployment.

A meteorology buoy (Fig. 1f) was deployed roughly 600 m to the SW of the primary horizontal array (Fig. 1b). It was instrumented with sensors to estimate the SHF and momentum flux (Supporting Information Table S1). Specifically, wind speed and direction, air temperature, relative humidity, downward longwave radiation, downward shortwave radiation,

water temperature at 0.5 m depth, and barometric pressure were measured, and averages stored every 10 min. The buoy was powered by two 80 A-h deep cycle marine batteries and charged by 4 20 W solar panels. SHF and momentum flux were estimated from the meteorological data using the algorithms of Fairall et al. (1996).

A spar buoy was deployed roughly 500 m to the NE of the primary horizontal mooring (Fig. 1b,f) in order to measure temperature structure close to the surface. It carried six TR-SOLO thermistors at depths of 1, 3, 5, 10, 15, and 20 m.

An ADCP mooring was deployed to the NW of the primary array (Fig. 1b,e). It carried an upward-looking Nortek Signature 500 ADCP at 60 m depth. The ADCP sampled at 4 Hz for 7 min every 53 min (7 min on, 46 min off) with a bin size of 4 m. Data were stored in raw beam coordinates. In addition, six TR-SOLO thermistors were placed on the line below the ADCP to provide higher vertical resolution than that provided by the h-mooring in the bottom half of the lake. Thermistor depths were 60–160 m in 20 m intervals.

Conductivity-temperature-depth (CTD) casts were taken with a Seabird 9 CTD on the deployment cruise, a mid-deployment survey cruise, and the recovery cruise. Sensors on the CTD platform included a Seabird SBE03 temperature sensor, a Digiquartz pressure sensor, an SBE43 oxygen sensor, WETLabs WETStar Chl *a* fluorescence and colored dissolved organic matter (CDOM) sensor, and a WETLabs C-STAR transmission sensor.

All figures are presented in Central Standard Time (UTC—6 h) so that noon roughly coincides with the highest levels of shortwave radiation. All data from this deployment are available in a public archive (Austin 2020).

### Meteorological setting

The site experienced a range of meteorological conditions during the deployment (Fig. 2).

Immediately following deployment, a large storm with strong winds from the NE blew through the region. This was followed by two more significant events later in May (Fig. 2a). The wind field was strongly polarized along a NE–SW axis (Fig. 2b,c), typical for this time of year, with the largest events oriented with winds blowing from the NE. The horizontal array was oriented largely along this axis (Fig. 1b). The large

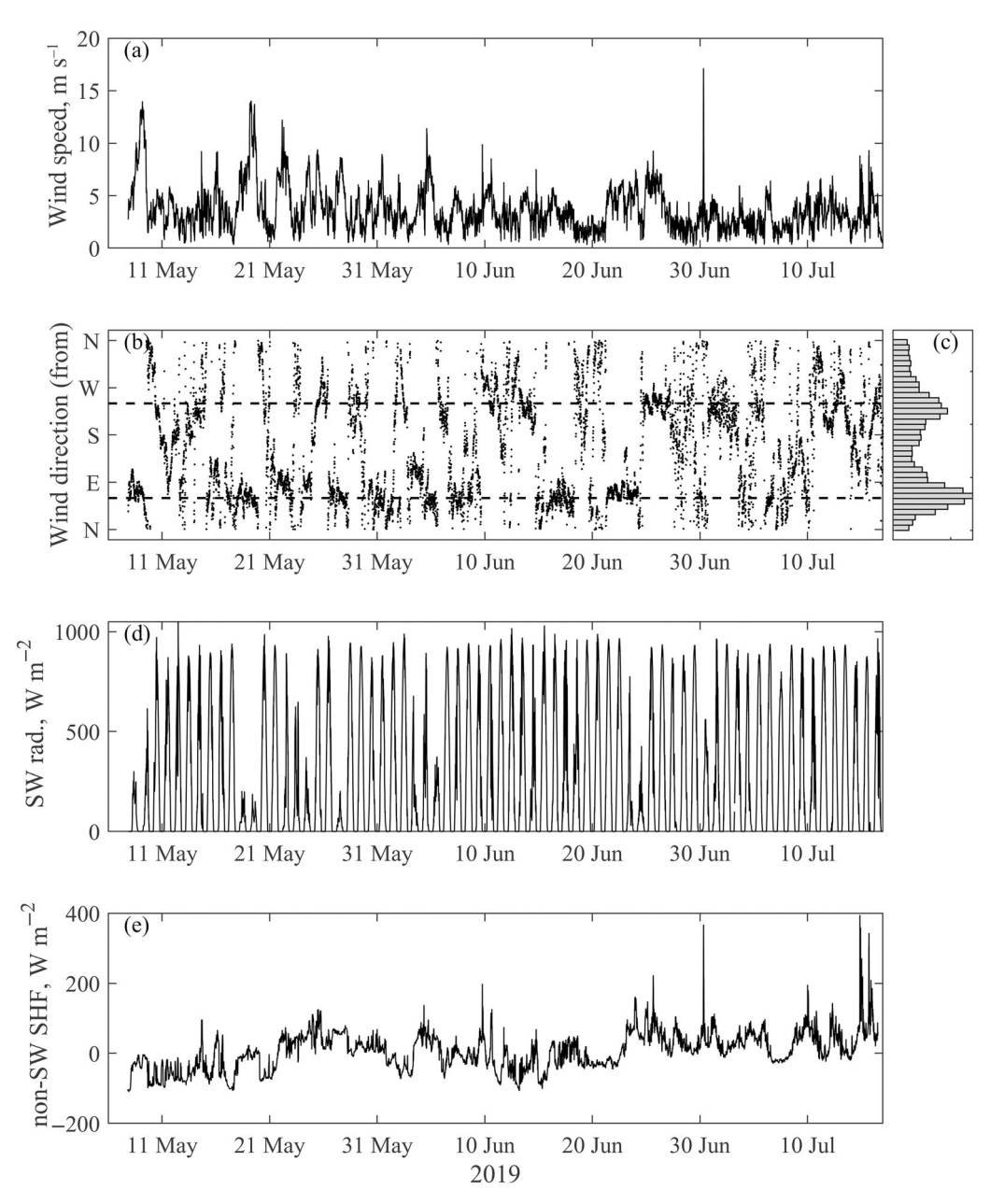


Fig. 2. (a) Wind speed, (b) wind direction, (c) wind direction histogram, by occurrence, (d) estimated downward shortwave radiation, and (e) sum of net longwave, sensible, and latent heat fluxes.

spike in wind speed observed on 30 June was observed by both anemometers. The deployment period spanned the summer solstice, so solar radiation was high throughout most of the experiment, with maximum clear-sky shortwave values on the order of  $1000~\rm W~m^{-2}$  at local noon (Fig. 2d). Several days throughout the experiment were cloudy as well, with maximum daytime shortwave values on the order of 200–  $300~\rm W~m^{-2}$ . Air temperature was typically greater than water temperatures, resulting in positive sensible and latent fluxes into the lake.

#### Thermal context

On 06 May, when the equipment was deployed, the site was still strongly negatively stratified, with a 100-m-thick layer of cool water overlaid on deeper water at approximately 3.1°C (Fig. 3a). This is distinct from the 2017 springtime convection season (Austin 2019), where the water column was fully mixed starting in early May 2017. Once the surface waters reached 3.1°C around 10 June, the water column was close to homogeneous, with warm water anomalies on the order of 0.1°C forming at the surface during daylight hours, and the water column homogenizing after sundown, with temperature differences over the entire water column less than 0.01°C as it

adjusted to neutral stability. During negative stratification, the surface water warmed at a rate of approximately  $0.05^{\circ}\text{C d}^{-1}$ , and during the period of neutral stratification at a rate of  $0.025^{\circ}\text{C d}^{-1}$ , roughly consistent with previous observations (Titze and Austin 2014; Austin 2019) and consistent with direct estimates of SHF. Around 05 July, the bottom of the water column reached the temperature of maximum density (about  $3.6^{\circ}\text{C}$  for 180 m depth) and the convective adjustment process no longer impacted the entire water column. Around 10 July, the surface reached  $T_{\text{MD}}$  and summer stratification starts to form. Equipment was recovered 6 d later, on 16 July.

# SHF and heat content

SHF was estimated using meteorological observations collected at the adjacent buoy. In the long-term mean, the net shortwave flux dominated the net longwave, latent, and sensible terms (Supporting Information Table S2), although instantaneously, the sum of the other three terms is at times significant compared to the shortwave term (Fig. 2e). The local water column heat content was estimated from a combination of thermistors on the ADCP mooring, the horizontal mooring, and the spar buoy, spanning the water column. This makes the assumption that, on the time scales of interest here,

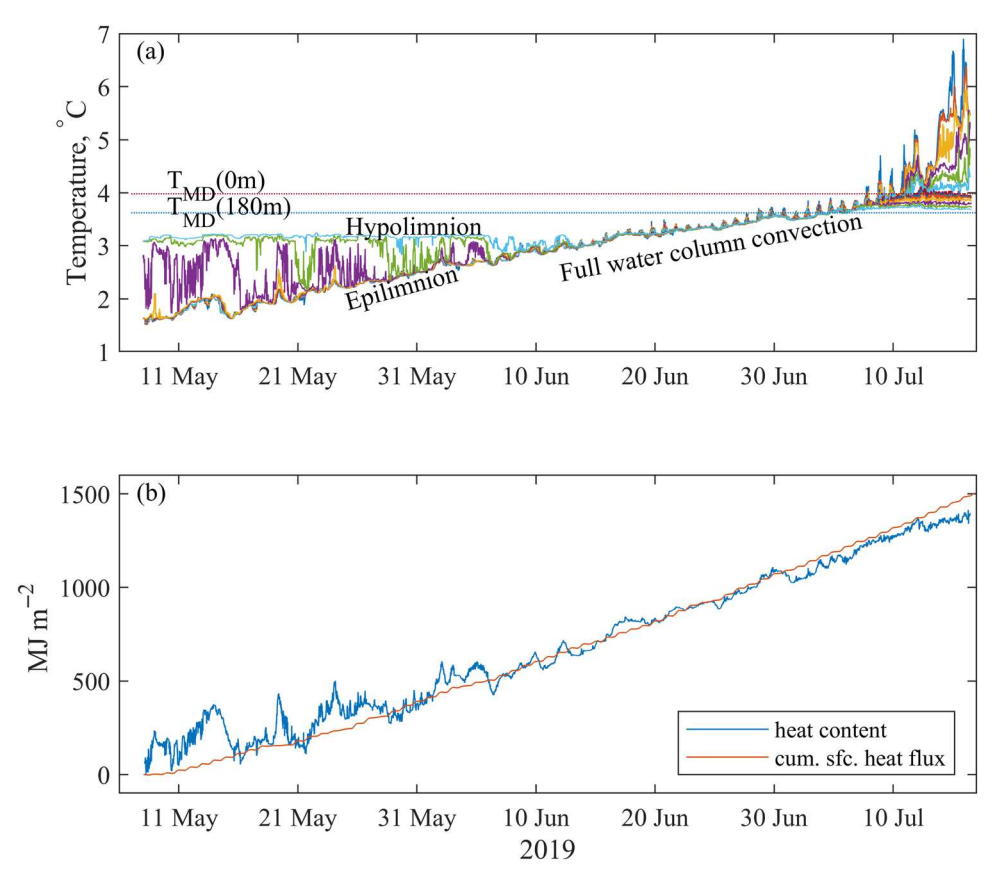


**Fig. 3.** (a) Temperature structure during 2019 deployment. Temperature of maximum density indicated for 0 m (surface) and 180 m (bottom). (b) Water column heat content (blue) and cumulatively integrated SHF (red).

horizontal variability between various moored components is negligible. The heat content (Fig. 3b) fluctuates significantly during the period of negative stratification, then settles into a roughly linear increase. The fluctuations during the negatively stratified period are due to variation in thermocline depth, due to passing internal waves. The time-integrated SHF (Fig. 3b) shows a rate of input of heat energy consistent with the stored heat. This suggests that, on short lateral scales, the system is reasonably one-dimensional, and that large-scale lateral advection of heat does not play a primary role in the local distribution of heat.

#### Currents

The ADCP measured currents in the top 54 m of the water column. Due to side-lobe interference, the shallowest bin was at approximately 10 m. The horizontal currents showed very little vertical structure, which is consistent with the well-mixed nature of the upper water column. Vertically averaged currents (Fig. 4a) are relatively weak, on the order of 0–5 cm s<sup>-1</sup>, with a deployment average of 3.5 cm s<sup>-1</sup>. Some evidence of near-inertial oscillations is present during the negatively stratified period, consistent with previous observations (Austin 2013). The flow is strongly polarized along a NE-SW axis, with flows to the SW dominating. There does not appear to be any straightforward relationship between the currents and the winds; that is, strong wind events are not necessarily accompanied by a strong response in the velocity field.

#### Discussion

## Observations from the horizontal mooring

Raw temperature data from the 18 thermistors along the headline display a number of different phenomena, the characteristics of which depend on the direction of the current. Highpassed temperature as a function of time is plotted in a waterfall plot for a 1-d period when the flow is largely oriented along the headline (Fig. 5a) and for a 1-d period when the flow is perpendicular to the headline (Fig. 5b). Data are plotted with a 0.05°C offset between adjacent thermistors, moving from SW to NE. During both periods, a clear diurnal signal is present, with anomalies starting to appear a few hours after sunup, peaking a few hours after local noon, and largely dissipating by local midnight. Anomalies are on the order of 0.1°C. In Fig. 6a, during which the flow is oriented largely along the headline, anomalies appear to propagate from the NE extent of the array to the SW extent. Some of the features appear to evolve with time, though this may be due to an imperfect alignment of the flow with the headline. A comparison of lagged correlation with measured current speed for periods of flow within 5° of the headline orientation (Supporting Information Fig. S1) shows that variability observed is dominated by lateral advection of temperature gradients. In contrast, the temperature observed during a period of flow perpendicular to the headline do not display these propagating features. Rather (Fig. 5b), features appear at a thermistor and perhaps one or two adjacent thermistors simultaneously.

This suggests that the flow field consists of a large-scale background flow with convective circulation superposed on it,

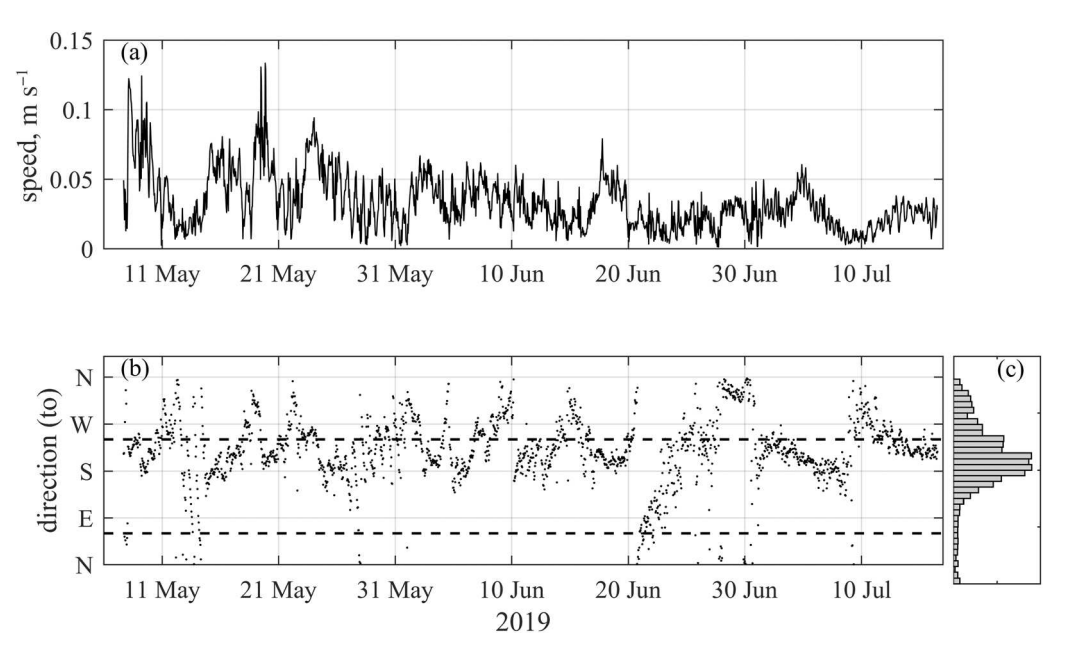


**Fig. 4.** (a) Vertically averaged (10–50 m) current magnitude, (b) vertically averaged current direction, with the orientation of the 2D mooring indicated as dashed lines, and (c) current direction histogram.

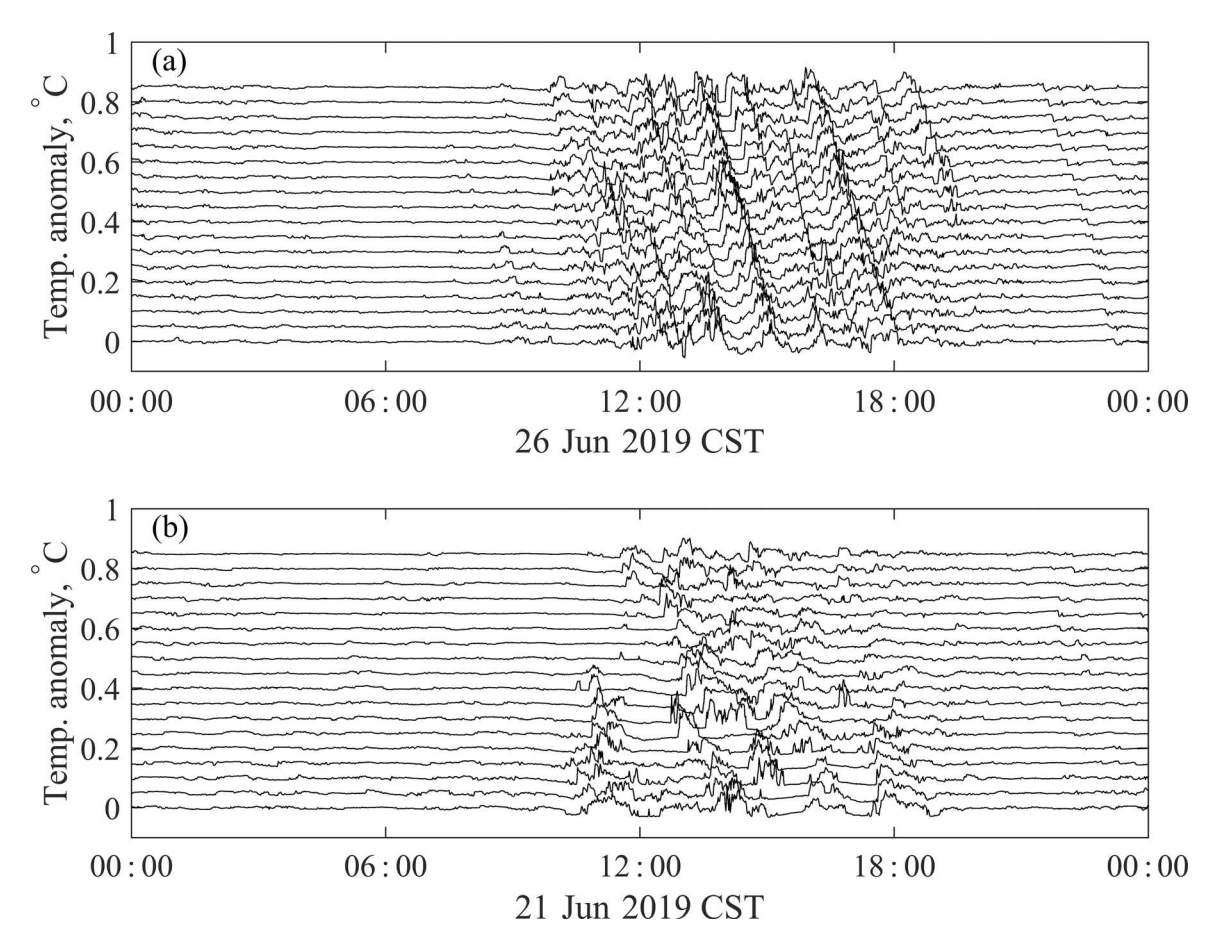


**Fig. 5.** (a) High-pass filtered (2.5 h cutoff) temperature from 18 headline thermistors from 1-d period in June during which flow is along headline. Thermistors offset by 0.05°C for the sake of clarity. Bottom traces are at the SW extent of headline. (b) Same but from a period of flow perpendicular to headline.

so that the slowly varying background flow advects parcels of anomalously warmed water past the moored array. In this case, horizontal velocities are dominated by the background flow, and vertical velocities by the convective circulation. Given the nature of the background flow, horizontal velocities measured at the ADCP are going to be representative of the horizontal velocity field in the vicinity of the h-mooring. However, convective cells have relatively short horizontal length scales (Austin 2019), and vertical velocities measured by the ADCP are not likely to be representative of the instantaneous vertical velocities in the vicinity of other elements of the moored array.

In order to interpret the data in the context of features being advected past the mooring, we can estimate several of the terms of the heat balance; we will show that the primary driver of temperature fluctuation at a point is lateral advection of horizontal gradients, which will allow a much more detailed perspective of lateral structure. The heat balance can be written

$$\frac{dT}{dt} = \kappa_{\rm T} \nabla^2 T + q(t, z),\tag{1}$$

where the material derivative is defined as

$$\frac{dT}{dt} = \frac{\partial T}{\partial t} + u \frac{\partial T}{\partial y} + v \frac{\partial T}{\partial y} + w \frac{\partial T}{\partial z},$$
 (2)

where  $\kappa_T$  is a diffusion constant, q represents external sources of heat, in this case solar radiation, and u, v, and w are velocity components in the x, y, and z directions, respectively. We have enough information to estimate some, but not all of these terms. We can estimate the locally observed rate of change term  $(\frac{\partial T}{\partial t})$  by taking a first difference at a chosen location (e.g., at  $x=10\,\mathrm{m}$ ). We can also estimate the advective term oriented in the direction of the headline  $(u\frac{\partial T}{\partial x})$  by differencing temperature from two thermistors on either side of the first thermistor (e.g.,  $x=0\,\mathrm{m}$  and  $x=20\,\mathrm{m}$ ) and combining that with velocity estimates from the ADCP. In order

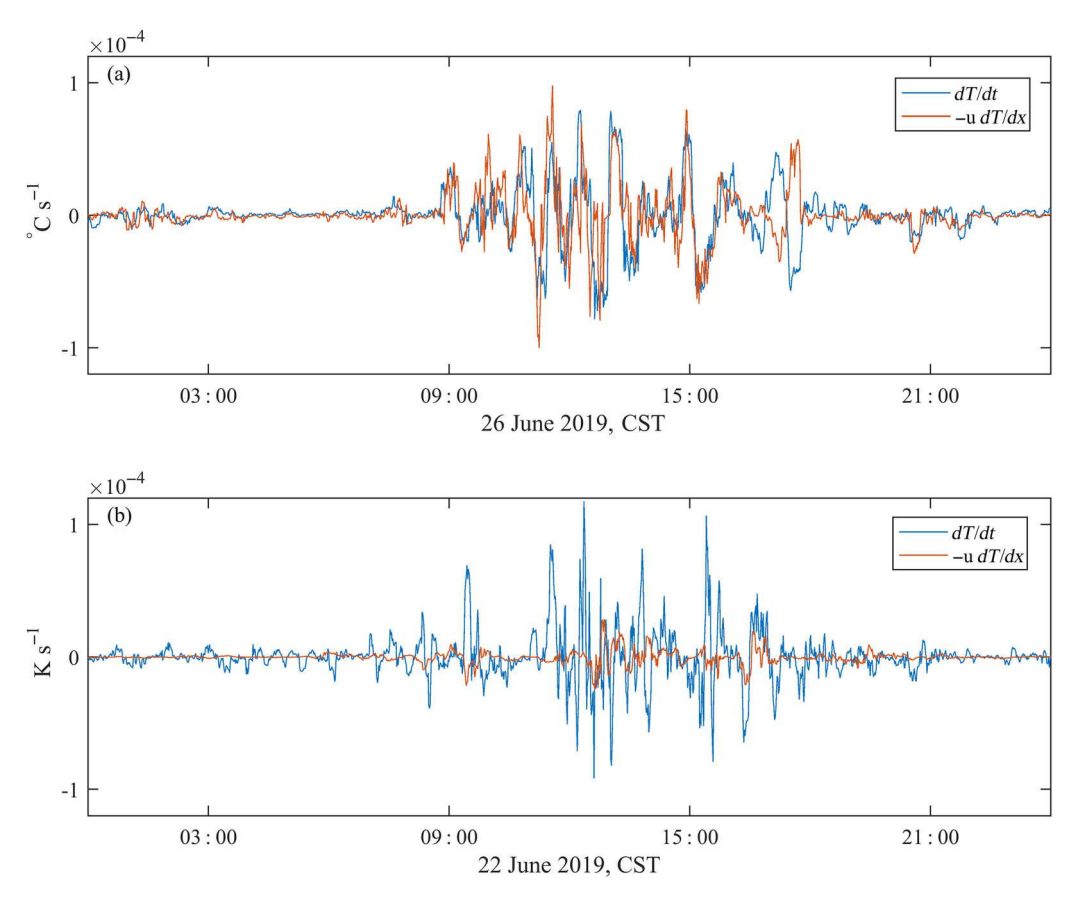


Fig. 6. (a) Local time rate of change and along-headline advection term during a period of flow along headline. (b) Same terms, during a period of flow perpendicular to headline.

to directly compare these two terms, the time rate of change term needs to be low-pass filtered to match with the scale of the advective term, which is set by the thermistor spacing. By choosing a period when the flow is closely aligned with the headline (i.e., a nonzero u, and  $v \approx 0$ ), where the x-coordinate lies along the headline and the y-axis is perpendicular, the advective term perpendicular to the headline  $(v\frac{\partial T}{\partial v})$  can be disregarded since  $v \approx 0$ . These two terms (Fig. 6a) compare favorably when done for a period with flow along the headline, although there is an instance at approximately 17:00 when the two terms strongly diverge; this may be due to a vertical advection event, where a descending plume directly impacts the central thermistor being used to determine  $\frac{\partial T}{\partial t}$ , then is advected toward the downstream thermistor, causing a drop in temperature at the central thermistor and a rise at the downstream, as observed. In contrast, the comparison is poor when done for a period when the flow is perpendicular to the headline (Fig. 6b). Similar analyses of other trios of thermistors during the same time periods and on other days of parallel or perpendicular flow (not shown) produces the same result, that is, there is nothing special about the set of thermistors (x = 0, 10, and 20 m) chosen for this figure. Days of a long-array flow

result in correlations between the time rate of change and advective term on the order of 0.5–0.6, whereas days of perpendicular flow result in correlations on the order of 0.1. In addition, it can be shown that the forcing term is several orders of magnitude smaller than either of these terms at this depth (although important near the surface). This suggests that the majority of instantaneous variability observed at a given location is due to the horizontal advection of strong lateral gradients in temperature. This balance is presumably true when flow is perpendicular to the headline as well, but we cannot estimate the perpendicular advective term since we do not have off-axis measurements of temperature.

Instantaneous variance in temperature at a given location, then, is due primarily to the advection of lateral temperature gradients regardless of the direction (with the caveat that there are, occasionally, events that contradict this, as in Fig. 6a at 17:00). This allows us to invoke a frozen field assumption, specifically, that locally observed changes in temperature are primarily due to advected horizontal gradients:

$$\frac{\partial T}{\partial t} \approx -\vec{u} \cdot \nabla_{\rm H} T. \tag{3}$$

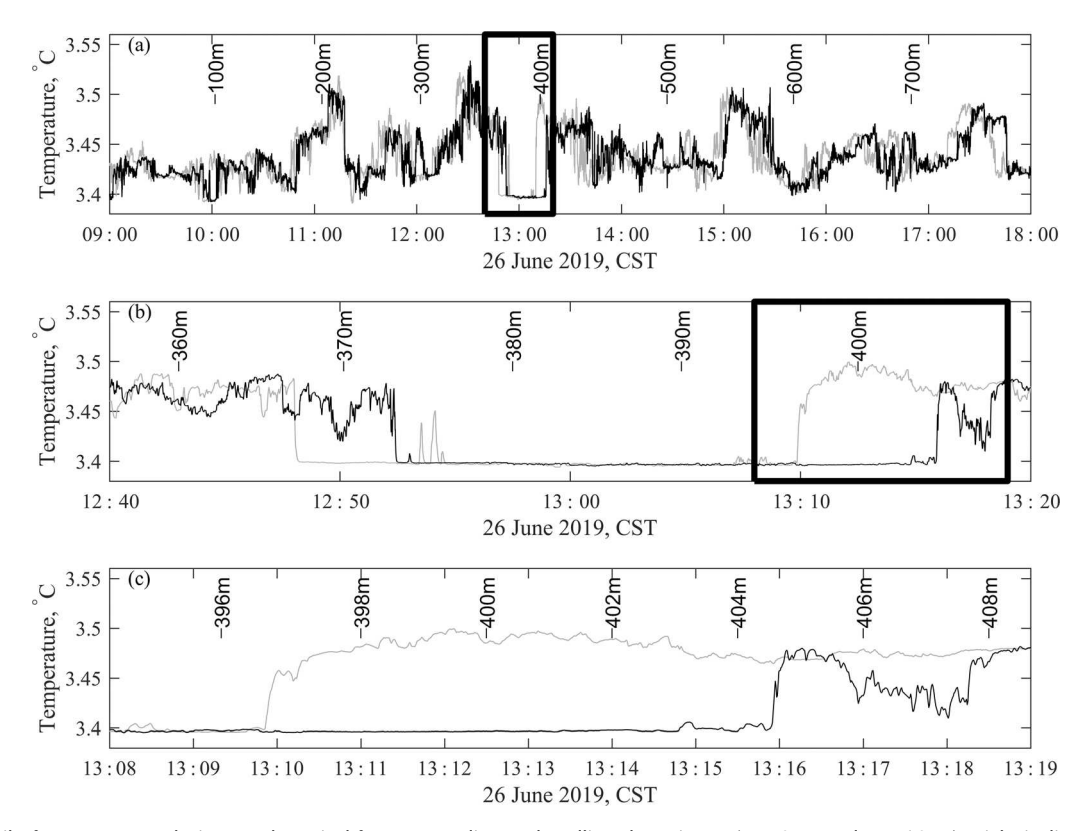


**Fig. 7.** (a) A detail of temperature during a 4-h period from two adjacent headline thermistors (x = 0 m and x = 10 m). Ticks indicate effective cumulative distance as measured by the ADCP to indicate rough lateral scale of features. Box outline period displayed in next frame. (b) Same as (a) but for a 40 min period. (c) Same as (b) but for a 9-min period.

This allows us to study the lateral structure of the warmed parcels at high spatial resolution. Given a temperature sample rate of 2 Hz and flows on the order of a few cm s<sup>-1</sup>, the effective spatial resolution is on the order of 2 cm s<sup>-1</sup>/2 Hz  $\sim$  1 cm, although we do not get to choose the horizontal direction in which this resolution exists. A representative 9-h segment of data from a pair of headline thermistors (34 m depth) (Fig. 7a-c) shows multiple examples of warm water anomalies passing by a pair of adjacent thermistors. While plotted as a function of time, the cumulative spatial displacement is shown with tick marks; the spacing of the tick marks is not constant because the velocity changes over the 4-h period. Anomalies are characterized by extremely sharp boundaries, with gradients on the order of 1°C m<sup>-1</sup>, and boundary widths (the transition region between cool ambient water and the warmer convective plume water) on the order of 10 cm. These features are sufficiently sharp to be up against the  $\sim 1$  s time constant of the sensors, and the true sharpness of the gradient may not be being captured entirely. The anomalies are set against a background of cooler, ambient water with very low levels of variance, whereas the temperature inside the anomalies tends to be comparatively noisy. The magnitude and width of the anomalies increases as the day passes. The offset between the two thermistors is approximately

consistent with the observed along-headline velocity of roughly  $2\ {\rm cm\ s^{-1}}$  and the  $10\ {\rm m}$  spacing between the thermistors.

We can extend this analysis by restricting it to periods of flow perpendicular to the headline and combining the thermistor and ADCP data to produce 2D synthetic images of temperature anomaly, with 10 m resolution along the headline and resolution on the order of centimeters perpendicular to the headline. To do so, we make the following assumptions: that the temperature exists over short periods of time as a "frozen field"; that is, changes to temperature following a parcel are small compared to lateral variability, and that the ADCP velocity data are largely representative of lateral velocities at the horizontal mooring. Then, we state

$$\vec{x}(t_0) = \vec{x}_0(t) + \int_{t_0}^{t_0} \vec{v}(t) dt,$$
 (4)

where  $\vec{x}_0$  are the fixed locations of the headline thermistors,  $\vec{x}(t_0)$  is the position of a water parcel at a fixed time  $t_0$ , and  $\vec{v}(t)$  is the horizontal velocity as measured by the ADCP. By combining this with the frozen field assumption, which can be stated as

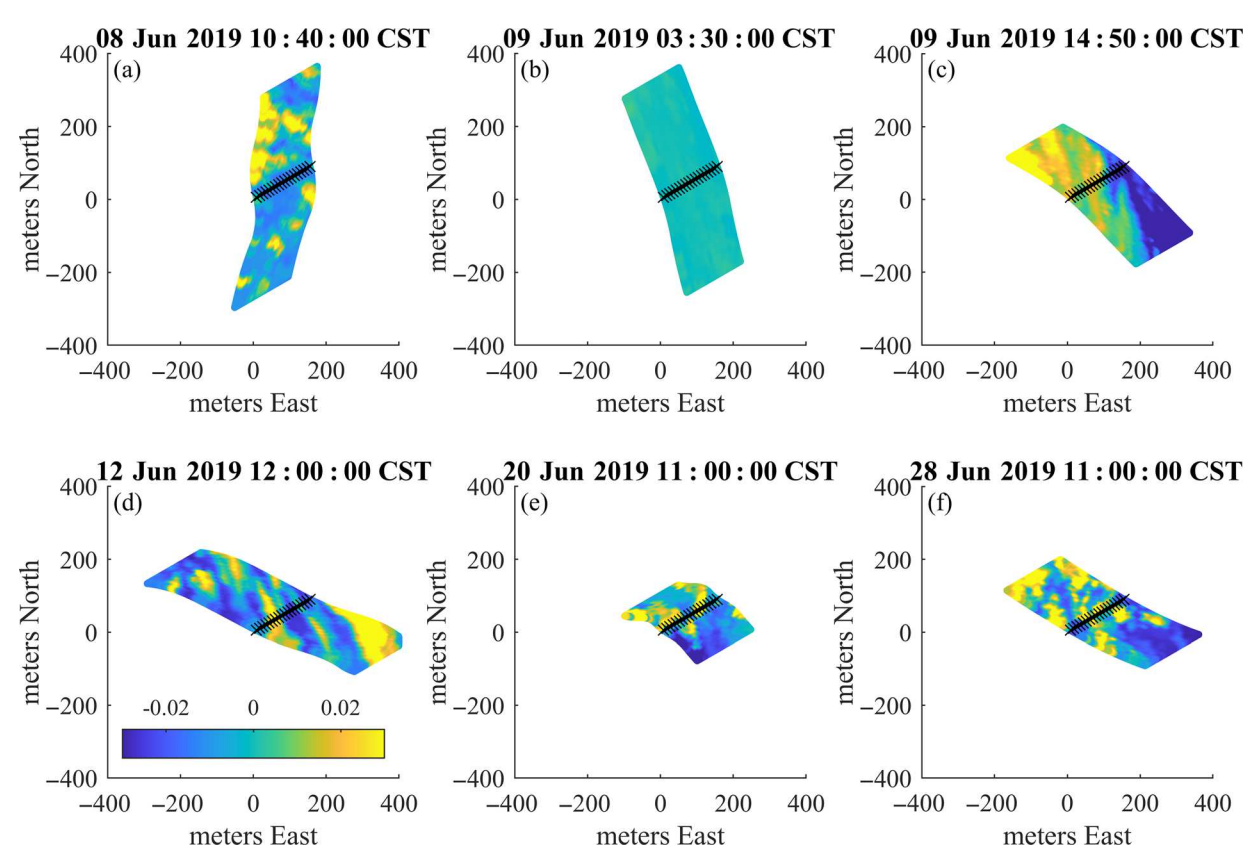


**Fig. 8.** 2D lateral structure of temperature anomaly at 34 m depth estimated using the frozen field assumption during six times: (**a**) 08 June, 10 : 40. (**b**) 09 June, 3 : 30. (**c**) 09 June, 14 : 50. (d) 12 June, 12 : 00. (e) 20 June, 11 : 00. (f) 28 June, 11 : 00. Temperature anomalies in °C.

$$T(\vec{x}, t_0) \approx T(\vec{x}_0, t),$$
 (5)

we can produce images of the temperature field in a 2D lateral "slice" to gain insight into the structure of the descending temperature anomalies (Fig. 8) integrating forwards and backwards 2 h from a central time. This method is most effective during periods when there is a significant component of steady flow perpendicular to the headline. When the flow is oriented along the headline, the synthetic spatial dimension and the orientation of the headline align. Due to the relative orientation of the mooring to the predominant current direction, most of the record consists of flow along the headline, resulting in few good 2D images. One way of envisioning this process is to consider the temperature distribution from the reference frame of the water; in that frame, the water is still, and the mooring is moving in the opposite direction through the water, measuring spatial variability over short spatial scales.

Six images are included here, picked as representative examples of different structures during periods when the flow had a significant component perpendicular to the headline. In these figures, the "x" markers represent the location of the headline thermistors. The velocity field was integrated forward and backward for 1 h around a central time, which is

displayed above the figure. Images where  $t_0$  is at night or very early in the morning, as expected, display very little structure, and display temperature ranges on the order of 0.01-0.02°C (Fig. 8b). However, daytime plots often display distinct structure. One common feature is "blobs" (Fig. 8a,e,f), which typically have scales on the order of tens of meters, roughly consistent with previous estimates (Austin 2019). Also frequently observed are "streaks" (Fig. 8c,d), in which roughly linear features with scales on the order of hundreds of meters are observed. There does not appear to be any obvious relationship between the wind direction and the orientation of the streaks. While we are not aware of other observational studies that have produced these 2D images, the basic lateral scales are consistent with previous work. Forrest et al. (2008) used an AUV to map temperature anomalies in Pavilion Lake during convection; finding similar scales to what is shown here, and also documented the advection of individual convective structures by a background flow. Using an approach similar to the one used here, van Haren and Dijkstra (2020) used a highly resolved point mooring to image convective cells (in the vertical) in Lake Garda, showing lateral scales on the order of 20 m.

We can estimate how long a parcel of water needs to stay at the surface to attain a given temperature anomaly. If we

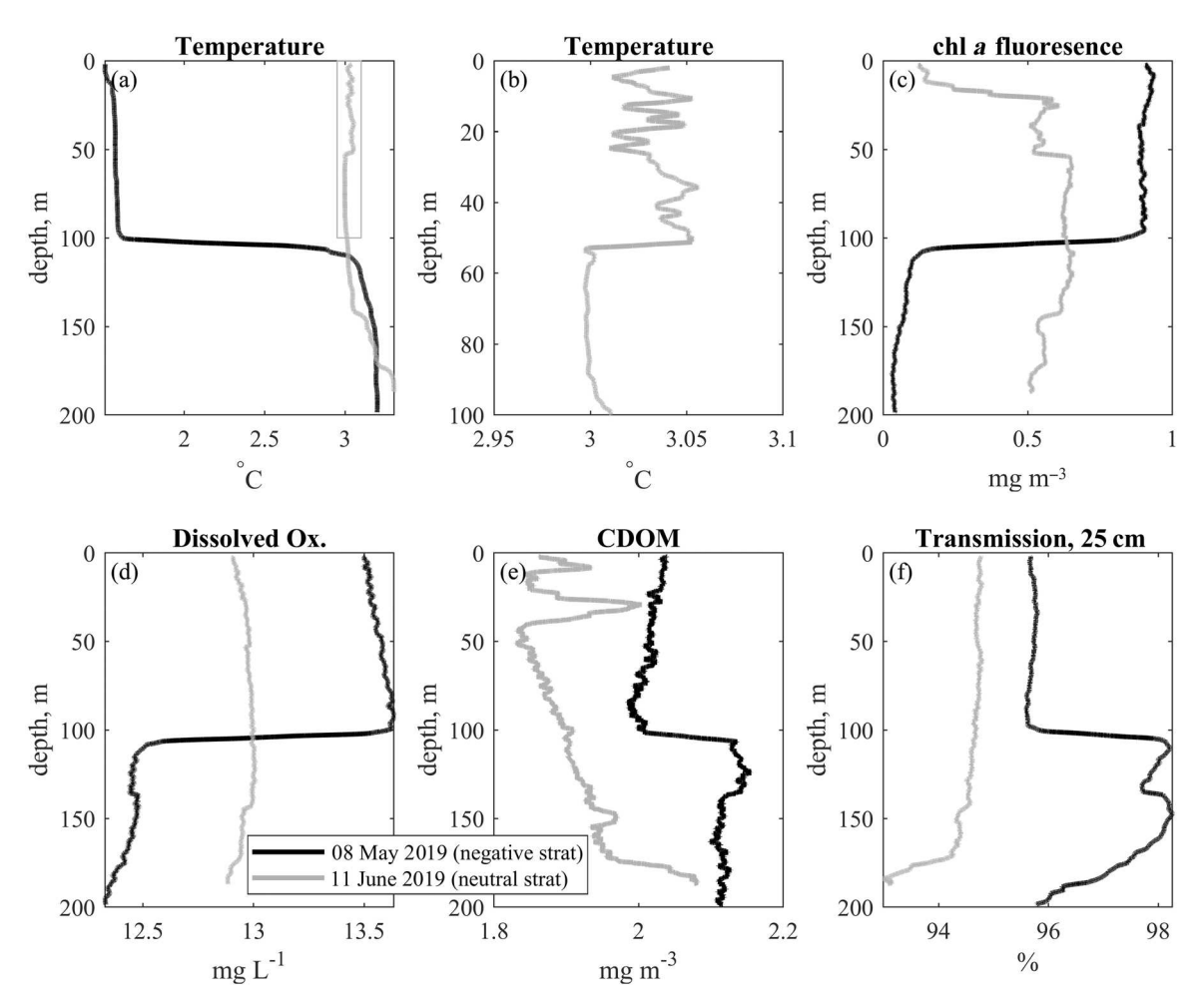


**Fig. 9.** Two CTD casts, one taken on 08 May 2019 during deployment and another on 11 June 2019 during a mid-deployment survey cruise. (**a**) Temperature; (**b**) detail of temperature in top 100 m from June cruise; (**c**) Chl *a* fluorescence; (**d**) dissolved oxygen, mg L<sup>-1</sup>; (**e**) CDOM; (**f**) beam transmission over 25 cm.

assume that the primary balance is heating due to solar radiation, the heat balance can be rearranged to yield

$$\Delta T = \frac{kI_0 e^{-kz}}{\rho c_p} \Delta t,$$

where  $\Delta T$  is the size of the temperature anomaly and  $\Delta t$  is the amount of time it takes to build up an anomaly of that magnitude. Using a noontime value of 1000 W m<sup>-2</sup> for  $I_0$ , a depth of 1 m, and  $k \sim 0.2$  m<sup>-1</sup>, an anomaly of 0.05°C would take roughly 20 min to form.

#### Impact on water quality parameters

Given the very small temperature differences addressed here, it is worth considering that, small as they are, they are a manifestation of a process that has a first-order impact on the distribution of water quality parameters. Temperature is nonetheless the primary field controlling density and hence the driving parameter behind convective readjustment. To

illustrate the impact of convection on the distribution of other water properties, two CTD casts, one taken during the deployment cruise on 08 May, and another taken during a mid-deployment survey cruise on 11 June and after the end of the negatively stratified period, show a significant shift in the distribution of water column properties. Two other CTD casts were taken during these periods but show the same trends and are omitted here for the sake of clarity. The temperature profile (Fig. 9a) shows a very sharp thermocline at about 100 m depth during the period of negative stratification, and a roughly uniform profile during neutral stratification. Chl a fluorescence shows a similar gradient at 100 m. The euphotic zone, with a 1% light level of about 25 m, is contained entirely in the upper layer so that photosynthesis is entirely absent in the lower level. After the onset of neutral stratification (Fig. 9a), the column-averaged Chl a fluorescence stays roughly the same but is now distributed over the entire water column by convective mixing (Fig. 9b). The anomalously low Chl a fluorescence in the top 20 m of the June profile is due to

daytime photobleaching rather than to low biomass. Dissolved oxygen (Fig. 9d) shows a similar pattern, with lower values in the lower portion of the water column during negative stratification, but relatively well-mixed over the water column thereafter, similar to Yang et al. (2017). CDOM is more complicated (Fig. 9e) but still shows a distinct shift at 100 m prior to the transition. There is a sharp jump in transmission (Fig. 9f) in the vicinity of the thermocline, but interestingly drops in both the upper and lower portions of the water column. The two casts are separated by more than a month, so there are likely other processes involved in modifying the transmission profile. Overall, however, these show that during negative stratification, convection keeps the top 100 m relatively well mixed with respect to several parameters, and the lower level is effectively isolated from the surface. During neutral stratification, convection is capable of rapidly distributing those same properties over the entire water column. The overall role this plays in determining ecosystem structure remains to be seen. Recent work (Austin et al. 2022) suggests that the shift in distribution of properties such as chlorophyll biomass can have a direct impact on zooplankton migratory behavior.

#### **Conclusions**

The short lateral scales of RDC presents novel convection present novel observational challenges. Horizontal scales on the order of tens of meters required a lateral array of thermistors, which when combined with velocity data from a nearby ADCP, provided insights into the nature of the temperature structure. The fact that the structures appear to be embedded in a background flow allowed the application of a "frozen field" assumption, allowing time to be used a proxy for lateral change. Given the relatively slow background flow and high rate of sampling, lateral structure on scales of centimeters was achieved, showing very sharp lateral boundaries between the cool, ambient waters and water recently warmed at the surface. Second, by combining velocity data with the horizontally resolved temperature data from the horizontal mooring, 2D images of temperature structure were constructed, demonstrating different sorts of structures such as streaks and relatively isotropic patches. Not enough data are available to start determining what sorts of forcing is behind these disparate structures. Finally, while the temperature anomalies are, in absolute terms, quite small, still result in vigorous mixing of the entire water column on relatively short time scales, which includes biologically relevant properties such as fluorescence and dissolved oxygen.

In a field campaign that has recently been completed, we modified the array, eliminated the vertical assemblies on the horizontal mooring, increased the horizontal resolution of the mooring, and added a highly resolved vertical mooring, similar to the work of van Haren and Dijkstra (2020), with 91 precision thermistors over the 180 m of the water column. These data will be considered in a subsequent manuscript. Future

fieldwork should also consider the impact of convective cells on the distribution of biogeochemical constituents. Effort should be made to make biogeochemical measurements that are highly resolved in both space and time, and that span various transitions in stratification state.

# Data availability statement

All data necessary to recreate this manuscript can be found at the Data Repository for the University of Minnesota (DRUM) at https://doi.org/10.13020/1XFM-MW95.

#### References

- Austin, J. A. 2013. Observations of near-inertial energy in Lake Superior. Limnol. Oceangr. **58**: 715–728. doi:10.4319/lo. 2013/58/2/0715
- Austin, J. A. 2019. Observations of radiatively driven convection is a deep lake. Limnol. Oceangr. **64**: 2152-2160. doi: 10.1002/lno.11175
- Austin, J. A. 2020. Radiatively driven convection, 2019 field campaign. Retrieved from the Data Repository for the Univ. of Minnesota. doi:10.13020/1XFM-MW95
- Austin, J. A. and C. Elmer. 2021. Lake Superior moored temperature and currents, Sep 2005–May 2015. Retrieved from the Data Repository for the Univ. of Minnesota. doi:10. 13020/zgw9-mk81
- Austin, J. A., T. R. Hrabik, and D. Branstrator. 2022. An abrupt decline in springtime zooplankton diel migration due to a shift in stratification regime. J. Great Lakes Res. **48**: 837–842 doi:10.1016/j.jglr.2022.03.011
- Boegman, L., J. Imberger, G. N. Ivey, and J. P. Antenucci. 2003. High-frequency internal waves in large stratified lakes. Limnol. Oceangr. **48**: 895-919.
- Bouffard, D., R. E. Zdorovennov, G. E. Zdorovennova, N. Pasche, A. Wüest, and A. Y. Terzhevik. 2016. Ice-covered Lake Onega: effects of radiation on convection and internal waves. Hydrobiologia **780**: 21–36. doi:10.1007/s10750-016-2915-3
- Butman, B., P. S. Alexander, A. Scotti, R. C. Beardsley, and S. P. Anderson. 2006. Large internal waves in Massachusetts Bay transport sediments offshore. Cont. Shelf Res. **26**: 2029–2049. doi:10.1016/j.csr.2006.07.022
- Cannon, D. J., C. D. Troy, Q. Liao, and H. A. Bootsma. 2019. Ice-free radiative convection drives spring mixing in a large lake. Geophys. Res. Lett. **46**: 6811-6820. doi:10.1029/2019GL082916
- Cannon, D. J., C. D. Troy, H. A. Bootsma, Q. Liao, and R.-A. MacLellan-Hurd. 2021. Characterizing the seasonal variability of hypolimnetic mixing in a large, deep lake. J. Geophys. Res. **126**: e2021JC017533. doi:10.1029/2021JC17533
- Fairall, C. W., E. F. Bradley, D. P. Rogers, J. B. Edson, and G. S.Young. 1996. Bulk parameterization of air–sea fluxes forTropical Ocean–Global Atmospheric Coupled-Ocean

- Atmospheric Response Experiment. J. Geophys. Res. **101**: 3747–3764.
- Farmer, D. M. 1975. Penetrative convection in the absence of mean shear. Quart. J. R. Met. Soc. **101**: 869-891.
- Forrest, A. L., B. E. Laval, R. Pieters, and D. S. S. Lim. 2008. Convectively driven transport in temperate lakes. Limnol. Oceanogr. **53**: 2321-2332.
- Gomez-Giraldo, A., J. Imberger, J. P. Antenucci, and P. S. Yeates. 2008. Wind-shear-generated high-frequency internal waves as precursors to mixing in a stratified lake. Limnol. Oceanogr. **53**: 354–367.
- Grosenbaugh, M., S. Anderson, R. Trask, J. Gobat, W. Paul, B. Butman, and R. Weller. 2002. Design and performance of a horizontal mooring for upper-ocean research. J. Atmos. Ocean. Technol. **19**: 1376–1389.
- Jonas, T., A. Y. Terzhevik, D. V. Mironov, and A. Wuest. 2003. Radiatively driven convection in an ice-covered lake investigated by using temperature microstructure technique. J. Geophys. Res. 108: 3183–3200. doi:10.1029/2002JC001316
- Kelley, D. E. 1997. Convection in ice-covered lakes: effects on algal suspension. J. Plankton Res. **19**: 1859–1880.
- Mironov, D., A. Terzhevik, G. Kirillin, T. Jonas, J. Malm, and D. Farmer. 2002. Radiatively driven convection in ice-covered lakes: Observations, scaling, and a mixed-layer model. J. Geophys. Res. **107**: 3032. doi:10.1029/2001JC000892
- Titze, D. J., and J. Austin. 2014. Winter thermal structure of Lake Superior. Limnol. Oceanogr. **59**: 1336–1348. doi:10. 4319/lo.2014.59.4.1336
- Ulloa, H. N., A. Wüest, and D. Bouffard. 2018. Mechanical energy budget and mixing efficiency for a radiatively heated ice-covered waterbody. J. Fluid Mech. **852**: R1. doi: 10.1017/jfm.2018.587
- van Haren, H., J. van Heerwaarden, R. Bakker, and M. Laan. 2016. Construction of a 3D mooring array of temperature sensors. J. Atmos. Oceanic Tech. **33**: 2247–2257.

- van Haren, H., and H. Dijkstra. 2020. Convection under internal waves in an alpine lake. Env. Fluid Mech. **21**: 305–316. doi:10.1007/s10652-020-09774-2
- van Haren, H., R. Bakker, Y. White, M. Laan, and J. van Heerwarden. 2021. Half a cubic kilometer mooring array of 3000 temperature sensors in the deep sea. J. Atmos. Ocean. Technol. **38**: 1585–1597. doi:10.1175/JTECH-D-21-0045.1
- Vehmaa, A., and K. Salonen. 2009. Development of phytoplankton in Lake Paajarvi (Finland) during under-ice convective mixing period. Aquat. Ecol. **43**: 693–705. doi:10. 1007/s10452-009-9273-4
- Volkov, S., S. Bogdanov, R. Zdorovennov, G. Zdorovennova, A. Terzhevik, N. Paslshin, D. Bouffard, and G. Kirillin. 2018. Fine scale structure of convective mixed layer in icecovered lake. Env. Fluid Mech. 19: 751–764. doi:10.1007/ s10652-018-9652-2
- Yang, B. J., L. B. Young, and M. Wells. 2017. High-frequency observations of temperature and dissolved oxygen reveal under-ice convection in a large lake. Geophys. Res. Lett. 44: 12218–12226. doi:10.1002/2017GL075373

#### Acknowledgments

The authors would like to thank Samuel Kelly, Alberto Scotti, and Stefan Llewellyn-Smith for fruitful conversations during the preparation of this manuscript, as well as the hard work of the crew of the R/V *Blue Heron*. Three anonymous reviews resulted in a significantly improved manuscript. Funding for the fieldwork and analysis was provided by NSF-OCE-1829895.

#### Conflict of interest

None declared.

Submitted 08 October 2021 Revised 01 April 2022 Accepted 19 July 2022

Associate editor: Leon Boegman